Acta Pharmaceutica Sinica B 2026;16(8):5471−5486

Chinese Pharmaceutical Association
Institute of Materia Medica, Chinese Academy of Medical Sciences

Acta Pharmaceutica Sinica B

www.elsevier.com/locate/apsb
www.sciencedirect.com

ORIGINAL ARTICLE

Metal-drug coordinated nanozymes for ROS scavenging and Kupffer cell polarization to alleviate drug-induced liver injury

Xiayun Chen[a,†], Ziqi Liang[a,†], Lichong Lu[a], Zhouchuan Shao[a], Wenhui Tang[a], Yiqi Liu[a], Jianqiao Li[b], Baizhong Chen[c], Enping Lai[a], Guodong Zheng[a,*], Minyan Wei[a,*], Shiying Li[a,*]

[a]*Guangdong Provincial Key Laboratory of Molecular Target & Clinical Pharmacology, The NMPA and State Key Laboratory of Respiratory Disease, The School of Pharmaceutical Sciences, Guangzhou Medical University, Guangzhou 511436, China*
[b]*Department of Emergency, The Second Affiliated Hospital of Guangzhou Medical University, Guangzhou 510260, China*
[c]*Guangdong Xinbaotang Biological Technology Co., Ltd., Jiangmen 529100, China*

Received 17 September 2025; received in revised form 27 November 2025; accepted 13 December 2025

KEY WORDS

Metal−drug coordination;
Drug delivery;
Nanozyme;
Anti-inflammatory;
Drug-induced liver injury;
ROS clearance;
Macrophage polarization;
Acute liver injury

Abstract Drug-induced liver injury (DILI) is a predominant cause of acute liver failure, intricately associated with excessive reactive oxygen species (ROS) production and the activation of inflammatory cascades. In this study, a metal−drug coordinated nanozyme (M-dCNs) is rationally designed to simultaneously scavenge ROS and polarize Kupffer cells to alleviate DILI. Specifically, the coordination between ferric ions (Fe^{3+}) and the complementary therapeutic agents of hesperetin (HST) and KPLH (KPLH1130) facilitates the formation of M-dCNs with uniform particle distribution and enhances structural stability. Notably, M-dCNs exhibits intrinsic antioxidant enzyme-mimetic activity, efficiently neutralizing intracellular ROS in damaged hepatocytes and thereby disrupting apoptosis-related signaling pathways. In parallel, M-dCNs synergistically reprograms hepatic macrophages toward an anti-inflammatory phenotype, leading to a marked reduction in pro-inflammatory cytokines such as tumor necrosis factor α (TNF-α) and interleukin 1β (IL-1β), and ultimately suppressing inflammatory cascades. *In vivo* studies demonstrate the hepatoprotective potential and therapeutic efficacy of M-dCNs in

*Corresponding authors.
E-mail addresses: gd200237@126.com (Guodong Zheng), weiminyan@163.com (Minyan Wei), lisy-sci@gzhmu.edu.cn (Shiying Li).
[†]These authors made equal contributions to this work.
Peer review under the responsibility of Chinese Pharmaceutical Association and Institute of Materia Medica, Chinese Academy of Medical Sciences.

https://doi.org/10.1016/j.apsb.2026.05.006

attenuating oxidative stress, reducing inflammatory cell infiltration, and restoring liver function. Collectively, this work presents a promising strategy for the treatment of DILI *via* the concurrent modulation of redox homeostasis and inflammatory microenvironment.

1. Introduction

Acute liver failure is a life-threatening condition marked by a spectrum of clinical manifestations, including coagulopathy, encephalopathy, and multi-organ dysfunction, with its etiology predominantly linked to viral infections, chronic alcohol consumption, and drug-induced toxicity[1,2]. Among these, drug-induced liver injury (DILI), particularly that caused by acetaminophen (APAP) overdose, has emerged as the leading cause of acute liver failure in clinical settings[3−5]. The underlying pathophysiological mechanism involves the excessive metabolism of APAP into the toxic intermediate *N*-acetyl-*p*-benzoquinone imine, which depletes hepatic glutathione (GSH) stores and triggers a cascade of oxidative stress through the overproduction of reactive oxygen species (ROS), ultimately resulting in hepatocellular necrosis[6−8]. In parallel, damage-associated molecular patterns released from necrotic hepatocytes activate resident Kupffer cells, leading to the secretion of pro-inflammatory cytokines and chemokines such as tumor necrosis factor α (TNF-α) and interleukin 1β (IL-1β), thereby promoting neutrophil infiltration and the recruitment of monocyte-derived macrophages into hepatic tissue[9−11]. Current treatment on DILI mainly focuses on hepatocytes detoxification. Taking the first line drug *N*-acetylcysteine (NAC) for example, NAC alleviates DILI by repleting glutathione (GSH) to neutralize the toxic metabolite *N*-acetyl-*p*-benzoquinone imine in hepatocytes. However, therapeutic efficacy is hindered by the excessive ROS generation once the GSH levels in hepatocytes are exhausted. Notably, excessive ROS levels have also been shown to skew Kupffer cells polarization toward the M1 phenotype macrophages in liver tissue, which is associated with heightened secretion of pro-inflammatory mediators that aggravate local inflammation and tissue injury[12−15]. Given the characteristics of ROS elevation and M1 macrophage activation in DILI, therapeutic interventions aimed at ROS scavenging for hepatocytes detoxification and Kupffer cells polarization to reprogram the inflammatory microenvironment hold substantial promise for the effective management of DILI.

Kupffer cells are the resident macrophages in liver, which can be classified into pro-inflammatory M1 and anti-inflammatory M2 phenotypes, and their inherent plasticity offers a promising strategy for alleviating inflammation associated with DILI[16−19]. To date, various chemical agents, including peroxisome proliferator-activated receptor gamma agonists, Toll-like receptor 4 antagonists, and AMP-activated protein kinase activators, have been shown to regulate macrophage polarization for treatments on repairing liver injury[20−23]. Especially, KPLH functions as a pyruvate dehydrogenase kinase (PDK) inhibitor that promotes M2 macrophage polarization and elicits potent anti-inflammatory responses, suggesting its great therapeutic potential for DILI[24,25]. Meanwhile, bioactive components and their metabolites originated from traditional Chinese medicine (TCM), have demonstrated great potent antioxidation and ROS elimination for hepatocytes detoxification, which have been applied for protection against liver injury[26−34]. Of note, hesperetin (HST) is a bioactive metabolite of hesperidin from TCM Tangerine peel, which exerts the Nrf2−NFκB pathway dependent antioxidant defense by ROS scavenging in drug injured hepatocytes[35−37]. It is assumed that the chemical agent KPLH and the TCM bioactive compound HST could synergistically improve the therapeutic efficacy of DILI by facilitating hepatocytes detoxification and Kupffer cells polarization. However, different pharmaceutical behaviors and unspecific targeting ability hinder their further application on DILI. To maximize the therapeutic efficacy, the co-delivery of synergistic agents KPLH and HST directly to DILI sites is crucial.

In recent years, self-assembled nanoparticles based on the bioactive compounds of TCM have attracted considerable interests in fields of drug delivery due to their carriers-free design[38,39]. Compared with the traditional drug delivery system, TCM bioactive compounds self-assembled nanoparticles are constructed by the bioactive compounds of TCM with molecular interactions, including hydrogen bonds, van der Waals forces and electrostatic attraction, thereby offering significant advantages on self-drug delivery, high drug loading efficacy and passive targeting ability[40]. Moreover, owing to their unique chemical structures and functional groups, some TCM bioactive compounds can strongly coordinate with transition metal (*e.g.*, Fe, Ce, Cu, Pt) to form nanozymes, which have been widely used for antioxidant defense on tumor therapy and different organ injury. These nanozymes exhibit SOD-, POD-, and CAT-like activities, catalytically decomposing ROS *via* redox cycling (*e.g.*, Fe^{2+}/Fe^{3+})[41−46]. Notably, our previous studies have demonstrated that metal ions can strongly coordinate with phenolic hydroxyl groups, facilitating the self-assembly of phenolic-containing drugs and enhancing their structural stability[47,48]. Considering the phenolic hydroxyl group of HST, we speculates that the TCM bioactive compound HST and Fe^{3+} might self-assemble as nanozymes due to the coordination between the phenolic hydroxyl structure and ferric ions, which would not only facilitate the hepatocytes detoxification by self-HST delivery, but also improve ROS clearance ability *via* nanozymes-like activities. Meanwhile, the nanozymes loaded with the anti-inflammatory inhibitor KPLH might accumulate on hepatic injured sites *via* natural uptake of Kupffer cells, thus enhancing ROS scavenge and Kupffer cells polarization for DILI treatment. However, the nanozymic catalytic potential of such metal-drug coordination nanomedicines has rarely been explored, and their therapeutic efficacy in DILI remains largely uninvestigated.

Taking the consideration above, a metal-drug coordinated nanozyme (M-dCNs) was developed to simultaneously scavenge ROS and polarize Kupffer cells for the effective alleviation of DILI. The coordination among ferric ions, HST and KPLH facilitated the formation of M-dCNs with uniform particle distribution and enhanced structural stability (Scheme 1A). Notably, M-dCNs exhibited intrinsic antioxidant enzyme-mimetic activity,

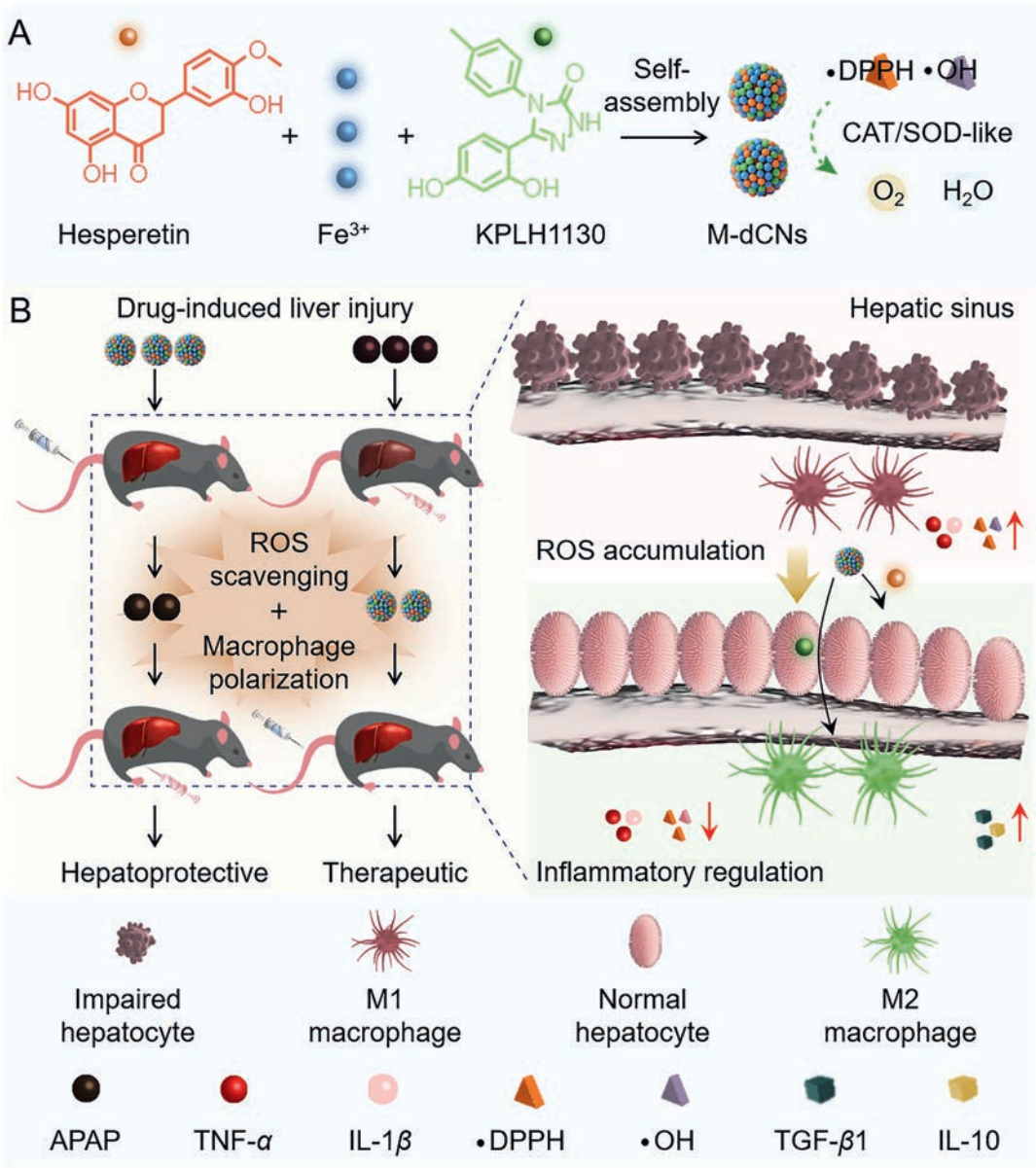

Scheme 1 Fabrication and the proposed mechanism of M-dCNs for DILI treatment. (A) The flavonoids compounds HST, macrophage polarized small molecule drugs KPLH, and ferric ion can self-assemble into the metal−drug coordinated nanozyme (M-dCNs) by coordination effect. (B) The mechanism of M-dCNs alleviates liver injury includes two aspects. On the one hand, HST exerts antioxidant effects in liver cells and pro-inflammatory macrophages, eliminating excessive accumulation of biological damage substances included ROS and DPPH in the liver. On the other hand, KPLH regulates the inflammatory environment by preventing macrophages from polarizing towards M1 type, further alleviating DILI.

enabling efficient neutralization of intracellular ROS within damaged hepatocytes and thereby interrupting apoptosis-associated signaling pathways (Scheme 1B). In addition, M-dCNs effectively reprogrammed hepatic macrophages toward anti-inflammatory phenotypes, resulting in a marked reduction in pro-inflammatory cytokines such as TNF-α and IL-1β and suppression of downstream inflammatory cascades. Both *in vitro* and *in vivo* evaluations confirmed the hepatoprotective potential and therapeutic efficacy of M-dCNs, as evidenced by significant histopathological repair of necrotic lesions, substantial inhibition of oxidative stress and inflammatory cell infiltration, and restoration of liver function. Collectively, this metal−drug coordinated nanozyme offers a promising strategy for mitigating liver injury through the concurrent modulation of redox homeostasis and the inflammatory microenvironment.

2. Materials and methods

2.1. Materials

HST and KPLH (Taoshu Biotechnology Co., Ltd., 50 mg, Shanghai, China). $FeCl_3{\cdot}6H_2O$ (Damao Chemical Reagent Factory, Tianjin, China). Alanine aminotransferase (ALT) and

aspartate aminotransferase (AST) detection kits (Jiancheng Bioengineering Research Institute, 96 T, Nanjing, China). 2,7-Dichlorofluorescein diacetate (DCFH-DA) (Futong Biotechnology Co., Ltd., 0.1 mL, Shanghai, China). Anti-CD206, inducible nitric oxide synthase (iNOS), CD80, Arginase 1 (Arg-1), and high mobility group box 1 (HMGB1) antibodies (Abcam plc, 50 μL, Cambridge, UK). AML12 (alpha mouse liver 12) cell line (Shanghai Institute of Cell Biology, 5×10^6 cells, Shanghai, China). Kupffer cells (WHELAB C2186) (WHELAB BIOSCIENCE Co., Ltd., 1×10^6 cells, Shanghai, China). Annexin V-FITC/PI apoptosis detection kit, catalase detection kit, total SOD activity detection kit, bicinchoninic acid protein assay kit, TNF-α and PDK ELISA kit (Beyotime Biotechnology Inc., 96 T, Shanghai, China). Dulbecco's modified Eagle's medium (DMEM) and fetal bovine serum (FBS) (Grand Island Biological Co., 500 mL, CA, USA). Penicillin streptomycin (Grand Island Biological Co., 100 mL, CA, USA). ITS (insulin + transferrin + selenium) (Grand Island Biological Co., 10 mL, CA, USA). Dexamethasone (MedChemExpress LLC, 25 mg, NJ, USA). Cy5.5 and DiR (MedChemExpress LLC, 10 mg, NJ, USA). Hydroxylamine hydrochloride, ortho phenanthrene and sodium acetate (Aladdin Biochemical Technology Co., Ltd., 1 g, Shanghai, China). DMSO (Macklin Biochemical Co., Ltd., 500 mL, Shanghai, China). •DPPH (MedChemExpress LLC, 25 mg, NJ, USA).

2.2. Cell culture medium

Kupffer cells were cultured in DMEM supplemented with 10% FBS and 1% penicillin streptomycin. AML12 cells from alpha mouse liver were cultured in DMEM containing 10% high-quality FBS, 1% ITS, 40 μg/L dexamethasone, and 1% penicillin streptomycin. The cells were stored in a humidified incubator at 37 °C and 5% CO_2 to ensure optimal growth conditions during the cultivation process.

2.3. Preparation and characterization of M-dCNs

2.3.1. Preparation of M-dCNs

1 mL of ultrapure water was added into a penicillin bottle, then 20 μL $FeCl_3 \cdot 6H_2O$ (10 mg/mL, dissolved in ultrapure water) and 30 μL HST (10 mg/mL, dissolved in DMSO) was added while stirring. After completion, 20 μL KPLH (10 mg/mL, dissolved in DMSO) was added and the stirring was continued for 9 min. The mixture was collected and centrifuged at 10,000×*g* (Eppendorf AG, 5810R, Hamburg, Germany) for 30 min. Finally, the precipitate in distilled water was obtained as M-dCNs and stored at 4 °C for further experiments. Cy5.5 labeled M-dCNs and DiR labeled M-dCNs were prepared by the same procedure of M-dCNs, in which KPLH was substituted to fluorescent dyes of Cy5.5 or DiR, respectively.

2.3.2. Characterization of M-dCNs

M-dCNs with different mass ratios of HST:Fe^{3+}:KPLH were synthesized, and 10 μL M-dCNs was dropped onto a copper mesh covered with a 1 carbon support film. The appearance was observed under a transmission electron microscope (TEM, JEOL Ltd., JEM1400PLUS, Tokyo, Japan). Zeta sizer Nano ZS90 analyzer (Malvern Instruments Ltd., Worcestershire, UK) was used to measure the particle size and zeta potential values of M-dCNs. TEM mapping was used to perform elemental analysis on M-dCNs.

2.3.3. The drug loading of M-dCNs

The content of Fe^{3+} in M-dCNs was determined by ortho phenanthroline spectrophotometry. 5 mL M-dCNs was accurately extracted and placed in 50 mL colorimetric tubes. 1 mL hydroxylamine hydrochloride solution (100.00 g/L) was added to each tube and shaken well. Then 2 mL ortho phenanthrene aqueous solution (1.50 g/L) and 5 mL sodium acetate solution (137.09 g/L) were added and diluted to the mark with distilled water. After 10 min, the absorbance of each solution was measured at a wavelength of 510 nm. Standard curve with Ferrous concentrations (ranging on 0−4 mg/L) with the same processes was used as the positive control. The iron content in M-dCNs was calculated based on the standard curve.

The content of HST and KPLH was determined by high-performance liquid chromatography (HPLC, Shimadzu Corp., LC-20AT, Kyoto, Japan) with eluents of H_2O + 0.1% HCOOH and CH_3CN + 0.1% HCOOH. HST solutions (5, 10, 50, 100, 200, 300 mg/L) and KPLH solutions (5, 10, 25, 50, 100, 200 mg/L) at various concentrations was prepared, and a standard curve was obtained using HPLC. In addition, M-dCNs was dissolved in DMSO and determined by HPLC. The peak areas corresponding to HST and KPLH were substituted into the standard curves to get the contents of HST and KPLH.

The 1000 Da dialysis bags were pre-equilibrated in phosphate buffered saline (PBS) buffers at pH 5.5 and pH 7.4, respectively. Subsequently, 2 mL of M-dCNs solution was loaded into each pretreated dialysis bag, which was then placed in a 50 mL centrifuge tube containing PBS buffer at the corresponding pH. The tubes were secured on an orbital shaker and incubated at 37 °C with constant shaking at 200 rpm (Eppendorf AG). Sampling was performed at predetermined time points (0, 5, 10, 15, 20, 30 min; 1, 2, 4, 6, 8, 12, 24, 36, 48 h) at each interval. 1 mL of the release medium was collected and immediately replaced with an equal volume of fresh PBS buffer at the same pH. The drug content in the samples was quantitatively analyzed by HPLC.

2.4. •DPPH scavenging ability

•DPPH was mixed with methanol to prepare a 0.1 mmol/L •DPPH solution. Subsequently, tested samples of HST, Fe^{3+}, KPLH, HST + Fe^{3+} + KPLH, and M-dCNs solutions were respectively mixed with •DPPH solution, and kept at room temperature in the dark for 30 min. The absorbance of each tested sample was measured at 517 nm. Samples substituted with distilled water and •DPPH solution were selected as the positive control. The •DPPH scavenging ability was calculated by the absorbances. Enzyme activity was determined according to the standard procedure of the reagent kit. The kinetic parameters, Km and Vmax, were measured as described in prior studies[55].

2.5. Hydroxyl radical scavenging ability

Tested samples including HST, Fe^{3+}, KPLH, HST + Fe^{3+} + KPLH, and M-dCNs were mixed with the working solution containing $FeSO_4$ (9 mmol/L), salicylic acid ethanol solution (2 mmol/L), and 0.03% H_2O_2 at a volume ratio of 5:4:4:4 in a colorimetric tube, respectively. The mixture was shaken well and heated in a 37 °C water bath for 15 min. The absorbance was detected at 510 nm. Samples substituted with distilled water and the working solution were selected as the positive control, and samples without the working solution were selected as the

negative control. The clearance rate was calculated by the following Eq. (1):

$$R\% = [A_0-(A_X-A_{X0})]/A_0 \times 100\% \quad (1)$$

where A_0 is the absorbance value of the positive control, A_X is the absorbance value of the tested samples, and A_{X0} is the absorbance value of the negative control.

2.6. Cellular uptake behavior

AML12 cells and Kupffer cells were respectively seeded and cultured into the confocal dishes with cell destiny of 1×10^6 per well overnight. Then, cells were incubated with Cy5.5 labeled M-dCNs (16.10 mg/L) for different incubation time (2, 4, and 8 h), respectively. Afterwards, the treated cells were washed with PBS thrice and stained with Hoechst for 30 min. Finally, intracellular fluorescence was observed using the confocal laser scanning microscopy (CLSM, Carl Zeiss AG, Zeiss LSM 880, Oberkochen, Germany). Meanwhile, cells were subjected to the same treatment and the fluorescence analysis was performed by a flow cytometer (Beckman Coulter, Inc., CytoFLEX S.4, CA, USA).

2.7. MTT assay

AML12 cells and Kupffer cells with the cell density of 1×10^4 per well were seeded onto the 96-well plates and cultured for 24 h, respectively. To investigate the biocompatibility of M-dCNs, cells were incubated with HST, Fe^{3+}, KPLH, HST + Fe^{3+} + KPLH, and M-dCNs (with HST concentrations ranging from 0.75 to 25.00 mg/L, Fe^{3+} concentrations ranging from 0.06 to 2.00 mg/L and KPLH concentrations ranging from 0.06 to 2.00 mg/L), respectively. After 24 h incubation, 20 μL of 3-(4,5-dimethyl-2-thiazolyl)-2,5-diphenyl-2*H*-tetrazolium bromide solution (MTT, 5 mg/mL) was added to each well and incubated for another 4 h. The culture medium was then replaced with 150 μL DMSO per well. Finally, the absorbance of each well was measured using a microplate reader (Thermo Fisher Scientific Inc., Varioskan ALF, DE, USA) at 570 nm. Cell viability was calculated by comparing the absorbance values between treated and untreated cell groups.

To investigate the *in vitro* hepatoprotection of M-dCNs, the AML12 cells were pretreated with HST, Fe^{3+}, KPLH, HST + Fe^{3+} + KPLH, and M-dCNs (with HST concentrations of 2.5 mg/L and KPLH concentrations of 0.2 mg/L) for 2 h, respectively. Afterwards, drug pretreated AML12 cells were incubated with 50 mmol/L APAP for 24 h. Finally, cell viability was measured by MTT assay with the same procedure mentioned above.

2.8. ROS detection

AML12 cells and Kupffer cells with the cell density of 1×10^6 per well were seeded into the confocal dishes and cultured for 24 h, respectively. Then, cells were separately pre-incubated with PBS, HST, KPLH, Fe^{3+}, HST + Fe^{3+} + KPLH, M-dCNs (11.67 mg/L (equivalent to HST concentration of 10.00 mg/L, KPLH concentration of 0.80 mg/L and Fe^{3+} concentration of 0.87 mg/L), 15 mg/L, 20 mg/L) and NAC (100 μmol/L) for 2 h, followed with another co-culture of APAP (15 mmol/L) for 8 h. After that, the treated cells were washed three times with PBS. Finally, the cells were incubated with the green probe DCFH-DA for ROS detection and observed by CLSM (Carl Zeiss AG). Cells without APAP treatment were selected as the control.

2.9. Cell apoptosis staining

AML12 cells with the cell density of 1×10^6 per well were seeded into the 6-well plates and cultured for 24 h, respectively. AML12 cells were separately incubated with PBS, HST, Fe^{3+}, KPLH, HST + Fe^{3+} + KPLH, and M-dCNs (equivalent to 2.50 mg/L HST, 0.20 mg/L KPLH, and 0.22 mg/L Fe^{3+}) for 2 h and stimulated with APAP (50 mmol/L) for another 24 h. Then, AML12 cells were collected and washed with PBS thrice, followed by fluorescent staining according to the instruction on Annexin V-FITC/PI apoptosis detection kit (Beyotime Biotechnology Inc.). Finally, a flow cytometer (Beckman Coulter, Inc.) was used to detect the cell apoptosis rates. AML12 cells without APAP treatment were chosen as the control.

2.10. Immunofluorescence staining

Kupffer cells with the cell density of 1×10^6 per well were seeded into the confocal dishes and cultured overnight. Then, cells were pretreated with lipopolysaccharide (LPS, 50.00 μg/L) for 24 h. Afterwards, the LPS pretreated cells were co-cultured with HST, Fe^{3+}, KPLH, HST + Fe^{3+} + KPLH, and M-dCNs (11.67 mg/L (equivalent to HST concentration of 10.00 mg/L, KPLH concentration of 0.80 mg/L and Fe^{3+} concentration of 0.87 mg/L), 15 mg/L, 20 mg/L) for another 24 h, respectively. Subsequently, cells were collected and separately incubated at 4 °C with anti-iNOS, anti-CD80, anti-Arg1, and anti-CD206 antibodies. After 12 h incubation, the cells were washed 3 times with PBS and stained with secondary antibody goat anti rabbit IgG labeled with Alexa Fluor 488 for 1 h in the dark. Finally, the cells were stained with DAPI dye and observed by CLSM (Carl Zeiss AG). Kupffer cells stimulated with LPS and interleukin 4 (IL-4, 50.00 μg/L) for 24 h were selected as the control.

2.11. Cytokine detection

Kupffer cells (1×10^6 per well) were seeded into the 6-well plates and cultured for 12 h. Kupffer cells were stimulated with LPS (50.00 μg/L) for 24 h. Then, LPS activated Kupffer cells were incubated with HST, Fe^{3+}, KPLH, HST + Fe^{3+} + KPLH, and M-dCNs (equivalent to 25.00 mg/L HST, 2.00 mg/L KPLH, and 2.18 mg/L Fe^{3+}) for another 24 h, respectively. LPS activated Kupffer cells without any other treatment were selected as the positive control. Kupffer cells stimulated with IL-4 (50.00 μg/L) for 24 h were selected as the negative control. Finally, the cell supernatant was collected to detect TNF-α or PDK levels by ELISA kit (Beyotime Biotechnology Inc.).

2.12. Western blotting

Kupffer cells (1×10^6 per well) were seeded onto the six-well plates and cultured for 24 h. After 24 h stimulation with LPS (50.00 μg/L), cells were separately incubated with HST, Fe^{3+}, KPLH, HST + Fe^{3+} + KPLH, and M-dCNs (equivalent to 25.00 mg/L HST, 2.00 mg/L KPLH, and 2.18 mg/L Fe^{3+}) for another 24 h, respectively. Then the treated cells were washed by PBS thrice and lysed with radio immunoprecipitation assay lysis buffer to extract the protein, followed by the detection by bicinchoninic acid protein assay kit (Beyotime Biotechnology Inc.). To

detect the expression of iNOS, proteins were separated by sodium dodecyl sulfate (SDS)-polyacrylamide gel electrophoresis and transferred to polyvinylidene fluoride membranes. The membranes were blocked with 5% non-fat milk, incubated with the primary antibody iNOS (Abcam plc) at 4 °C overnight, then followed by another 1 h incubation with horseradish peroxidase-conjugated secondary antibody (Abcam plc) at room temperature. Finally, the protein bands were imaged by a chemiluminescence system (GE HealthCare Technologies Inc., Amersham Imager 600, Chicago, USA). Kupffer cells stimulated with LPS or IL-4 (50.00 μg/L) only were selected as controls. β-Actin was chosen as an endogenous reference.

2.13. Biodistribution of M-dCNs

All animal experiments were conducted in accordance with the Regulations on the Administration of Laboratory Animal Affairs and approved by the Institutional Animal Care and Use Committee of the Animal Experiment Center of Guangzhou Medical University (Approval number: GY2024-448). Healthy female C57BL/6J mice (18−20 g, 6−8 weeks) were randomly divided into two groups (4 mice per group). Then, DiR labeled M-dCNs (4.05 mg/kg) was administrated into the mice *via* tail vein injections. At specific time intervals (0.5, 4, 8, 12, and 24 h), the treated mice were euthanized with isoflurane, and imaged by the small animal optical *in vivo* imaging system (PerkinElmer, Inc., IVIS Lumina XRMS, Massachusetts, USA). At 24 h postinjection, the treated mice were sacrificed and their main organs (including hearts, livers, spleens, lungs, and kidneys) were collected for *ex vivo* imaging. Subsequently, CD11b and transferrin fluorescence staining on liver tissue slices was performed to observe the co-localization of DiR labeled M-dCNs with hepatocyte and Kupffer cells.

2.14. Hepatoprotective effect of M-dCNs on early DILI

C57BL/6J mice were randomly divided into 7 groups ($n = 4$). Saline, HST (10.00 mg/kg), Fe^{3+} (0.87 mg/kg), KPLH (0.80 mg/kg), HST (10.00 mg/kg) + Fe^{3+} (0.87 mg/kg) + KPLH (0.80 mg/kg), and M-dCNs (11.67 mg/kg) were injected into the tail vein of mice, respectively. After 2 h of administration, APAP (350.00 mg/kg) was intraperitoneally injected into the treated mice to form an acute liver injury model. At 24 h postinjection of APAP, whole blood of the treated mice was collected from hearts and centrifuged at 5000×*g* for 15 min to obtain the serum. Reagent kit was used to detect the levels of ALT and AST in the serum. Liver tissue was collected and investigated by hematoxylin and eosin (H&E) staining. Next, liver cell necrosis, infiltration, inflammation and area of pathological regions in H&E sections of mice were estimated using software Image J. Moreover, liver tissues were stained for immunofluorescence with HMGB1, TNF-α, IL-1β, nicotinamide adenine dinucleotide phosphate oxidase 2 (NOX2), CD206, interleukin 10 (IL-10) and transforming growth factor β1 (TGF-β1), and the intracellular fluorescence were detected and analyzed by CLSM.

2.15. Therapeutic effect of M-dCNs on advanced DILI

To establish the advanced DILI model, C57BL/6J mice (18−20 g, 6−8 weeks) were randomly divided into 7 groups ($n = 4$) and intraperitoneally injected by APAP (350.00 mg/kg). After 3 h treatment of APAP, mice were injected with HST (10.00 mg/kg), Fe^{3+} (0.87 mg/kg), KPLH (0.80 mg/kg), HST (10.00 mg/kg) + Fe^{3+} (0.87 mg/kg) + KPLH (0.80 mg/kg), or M-dCNs (11.67 mg/kg, 15 mg/kg, 20 mg/kg) or NAC (300 mg/kg) *via* the tail vein. The same volume of saline was administrated to mice in the healthy control group and advanced DILI control group. After 24 h postinjection of APAP, the treated mice were euthanized by isoflurane. Then, whole blood was collected from their hearts and centrifuged at 5000×*g* for 15 min to obtain the serum. Levels of ALT and AST in the serum were detected by the ALT and AST activity assay kits, respectively. Liver tissue was harvested, fixed in formalin, and embedded in paraffin, sliced, and stained by H&E. Next, area of pathological regions in H&E sections of mice including hepatocyte necrosis, infiltration, and inflammation were estimated using software Image J. Moreover, liver tissues were separately stained with fluorescent antibodies including HMGB1, TNF-α, IL-1β, NOX2, CD206, IL-10 and TGF-β1 for immunofluorescence, and intracellular fluorescence was detected and analyzed by CLSM.

2.16. Biosafety of M-dCNs

Healthy C57BL/6J mice (18−20 g, 6−8 weeks) were randomly divided into 6 groups ($n = 4$) and injected with HST (10.00 mg/kg), Fe^{3+} (0.87 mg/kg), KPLH (0.80 mg/kg), HST (10.00 mg/kg) + Fe^{3+} (0.87 mg/kg) + KPLH (0.80 mg/kg), or M-dCNs (11.67 mg/kg) *via* tail vein. After 24 h of injection, the mice were euthanized by isoflurane and whole blood was collected for biochemical testing. Levels of ALT, AST in serum were detected by ALT and AST activity assay kits, and levels of UREA and uric acid (UA) in serum were analyzed by a fully automatic blood biochemical analyzer. Major organs (including hearts, livers, spleens, lungs, kidneys) were harvested and assessed by H&E staining. After intravenous injection of M-dCNs at varying doses (11.67, 15, and 20 mg/kg), major organs were collected from mice on days 7 and 14 for H&E staining, while blood samples were obtained for biochemical assessment of AST, ALT, creatinine (CRE), and bilirubin levels. Female C57BL/6J mice received intravenous injections of either free DiR or DiR-labeled M-dCNs *via* the tail vein. Blood samples were collected from the orbital venous plexus at 0.08, 0.25, 0.5, 1, 2, 8, and 24 h post-injection, and the concentration of DiR in the blood was measured using a microplate reader.

2.17. Statistical analysis

GraphPad Prism 8 software (Prism, USA) was used to analyze the data. All data are presented as mean ± standard deviation (SD). Statistical analysis was conducted using one-way ANOVA, with $P < 0.05$ indicating statistically significant differences.

3. Results and discussion

3.1. Synthesis and characterization of M-dCNs

In light of the elevated ROS levels and predominance of M1 macrophages in DILI, the antioxidant agent HST and the anti-inflammatory compound KPLH were employed to construct the M-dCNs. The phenolic hydroxyl groups present in both HST and KPLH were hypothesized to coordinate with ferric ions, thereby promoting nanozyme assembly. Free HST was found to exhibit

poor solubility in water, however, its aqueous solubility was markedly improved upon coordination with ferric ions (Supporting Information Fig. S1A). A screening of metal ions revealed that iron ions demonstrated superior coordination capability and yielded more uniform nanoparticles compared to zinc and copper ions at the same feed ratio (Fig. S1B−S1E). Moreover, the coordination between iron ions and HST was shown to maintain good stability in aqueous solution over a period of seven days (Fig. S1F−S1H). Based on these findings, iron ions were selected for further study. Subsequent investigations indicated that the optimal particle size and stability were achieved when the mass feed ratio of HST to iron ions was maintained at 3:2 (Supporting Information Fig. S2A−S2J). To optimize the coordination interactions, the metal-drug complexation among Fe^{3+}, HST, and KPLH was systematically evaluated at various feed mass ratios. As shown in Fig. 1A−D, dynamic light scattering and TEM confirmed successful nanoparticle formation, indicative of strong coordination interactions. Notably, a mass ratio of HST:Fe^{3+}:KPLH at 3:2:2 yielded uniformly spherical nanoparticles with minimal changes in hydrodynamic diameter and polydispersity index (PDI) over time in aqueous solution, demonstrating excellent colloidal stability (Fig. 1E). M-dCNs demonstrated favorable stability for over 96 h in DMEM containing 10% FBS and in pH 7.4 buffer, indicating its capacity to retain structural integrity and functional effectiveness in biological environments (Supporting Information Fig. S3A and S3B). Under acidic conditions (pH 6.5 and 5.0), M-dCNs exhibited aggregation behavior (Fig. S3C and S3D), consistent with previous literature reports[49−51]. Moreover, all M-dCNs formulations showed a consistently negative zeta potential around −16 mV (Supporting Information Fig. S4A). Elemental mapping *via* TEM-energy-dispersive X-ray spectroscopy (TEM-EDS) further validated the co-localization of C, N, O, and Fe elements within M-dCNs, confirming successful metal-ligand coordination (Fig. 1F and G). To elucidate the self-assembly of M-dCNs, ultraviolet−visible (UV−Vis) spectroscopy was performed under varying ionic and hydrophobic conditions. No significant spectral shifts were observed with increasing NaCl concentration, whereas a slight red-shift in the absorption peak was induced by SDS, suggesting the presence of hydrophobic interactions among the assembled drug components (Fig. S4B and S4C). Additionally, Fourier-transform infrared spectroscopy revealed red-shifting

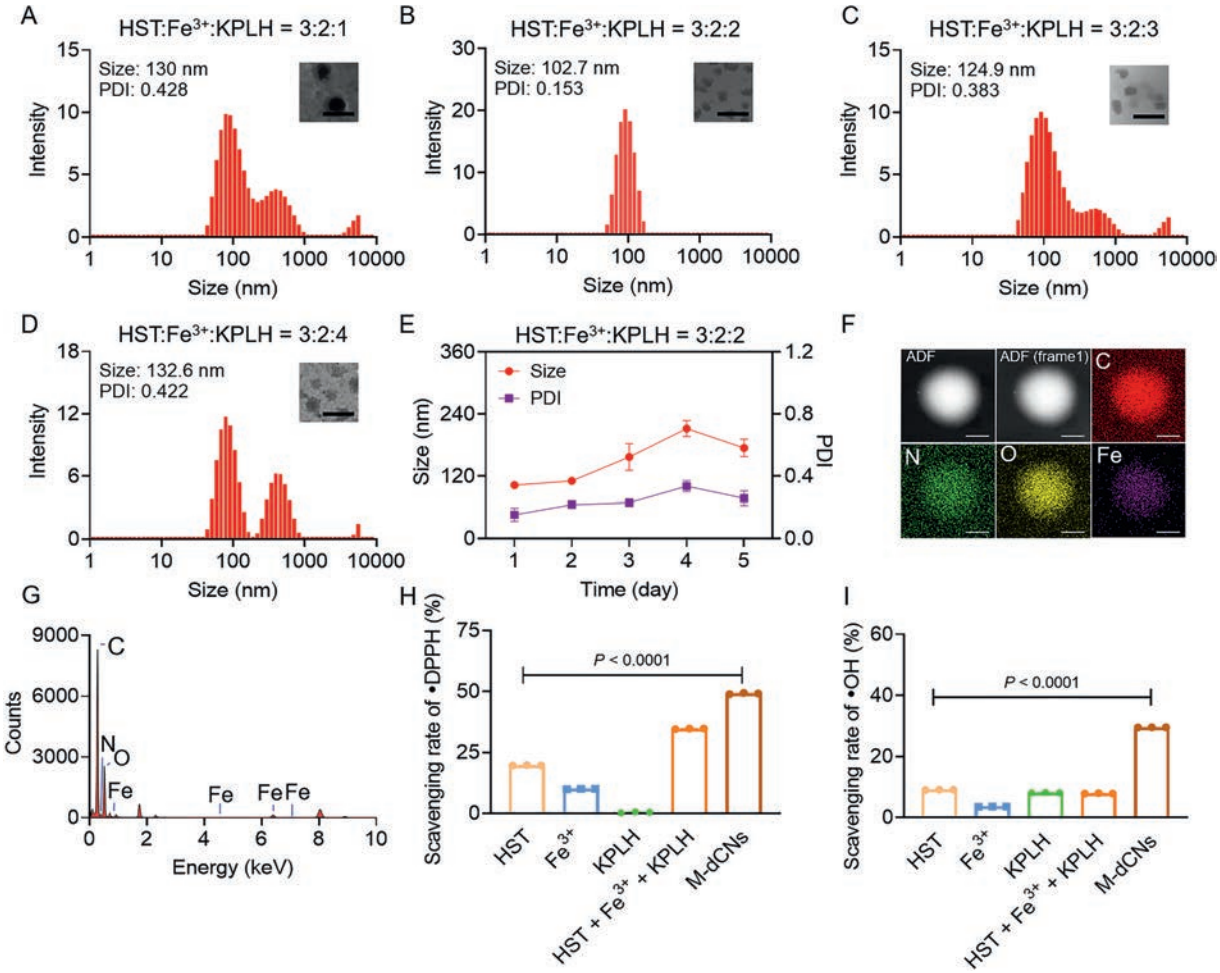

Figure 1 Fabrication and characterization of M-dCNs. Particle size distributions and TEM image (insert) obtained based on the assembly of HST, Fe^{3+}, and KPLH at the mass ratios of (A) 3:2:1, (B) 3:2:2, (C) 3:2:3, or (D) 3:2:4. Scale bar = 200 nm. (E) The changes of particle size and PDI of M-dCNs in 5 days at the ratios of 3:2:2 (n = 3). (F) The element mapping image of M-dCNs. Scale bar = 200 nm. (G) The relative elemental composition distribution obtained from TEM-EDS. The ability of M-dCNs to clear (H) •DPPH or (I) •OH *in vitro* (n = 3). Data are presented as mean ± SD. P values were tested *via* a one-way ANOVA analysis.

of C═O and −OH stretching vibrations by 22 cm^{-1} and 3421 cm^{-1} in M-dCNs compared to free HST/KPLH, further indicating coordination bonding *via* these functional groups (Fig. S4D). The contents of HST and KPLH in M-dCNs were quantified by HPLC (Supporting Information Table S1). Prior to sample analysis, the method was validated by assessing its intra-day accuracy, precision, repeatability, recovery rate, and stability. As shown in Supporting Information Tables S2−S4, the chromatographic conditions exhibited possess excellent precision (relative standard deviation (RSD) < 3%), accuracy (RSD <3%), and stability (RSD <3%). All validated parameters met the criteria for routine analysis, confirming that the method was suitable for reliable and accurate quantification of M-dCNs. Finally, drug loading was quantified *via* HPLC and *o*-phenanthroline spectrophotometry, revealing encapsulation efficiencies of 85.70% for HST, 7.50% for KPLH, and 6.80% for Fe^{3+} Supporting Information Fig. S5A-S5E and Table S5). The drug release profile of M-dCNs was investigated under physiological conditions and in buffer solutions at different pH values. As depicted in Supporting Information Fig. S6A and S6B, both HST and KPLH were released from M-dCNs at pH 5.5 and 7.4 (25 °C). Within 48 h, the cumulative drug release reached 64.8 ± 3.2% and 60.6 ± 3.6% for HST, and 72.9 ± 2.1% and 62.8 ± 4.5% for KPLH, respectively. Notably, drug release from M-dCNs was faster at pH 5.5 than at pH 7.4, a characteristic considered beneficial for their therapeutic action in the acidic microenvironment of injured liver tissue. Additionally, under physiological conditions (pH 7.4, 37 °C), drug release was more

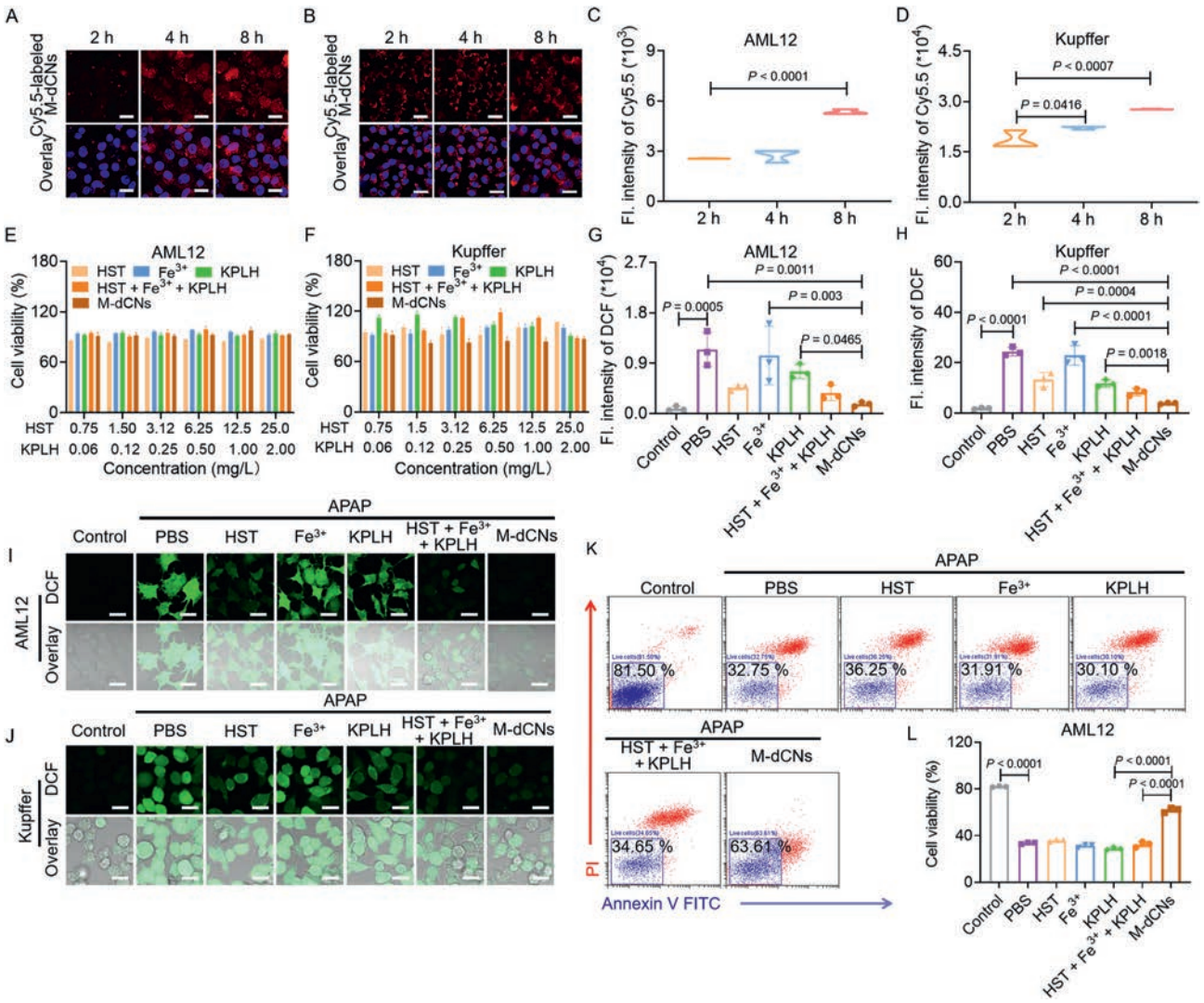

Figure 2 Cellular uptake behavior of M-dCNs and ROS clearance activity. Representative CLSM images of (A) AML12 and (B) Kupffer cells after treatment with Cy5.5-labeled M-dCNs at different times (2, 4, and 8 h). Scale = 40 μm. The flow cytometry analysis of (C) AML12 and (D) Kupffer cells after those treatments (n = 3). Cell viabilities of (E) AML12 or (F) Kupffer cells after treatment with HST, Fe^{3+}, KPLH, HST + Fe^{3+} + KPLH or M-dCNs. Intracellular ROS measurement of (I) AML12 or (J) Kupffer cells and (G, H) corresponding quantitative fluorescence analysis after treatment with HST, Fe^{3+}, KPLH, HST + Fe^{3+} + KPLH or M-dCNs in the presence of APAP by using DCFH-DA as ROS probe. Scale bar = 40 μm. (K) Representative diagram of flow cytometry and (L) corresponding quantitative fluorescence analysis of AML12 cells treated with HST, Fe^{3+}, KPLH, HST + Fe^{3+} + KPLH130 or M-dCN in the presence of APAP and stained with PI/Annexin V-FITC (n = 3). Data are presented as mean ± SD. P values were tested *via* a one-way ANOVA analysis.

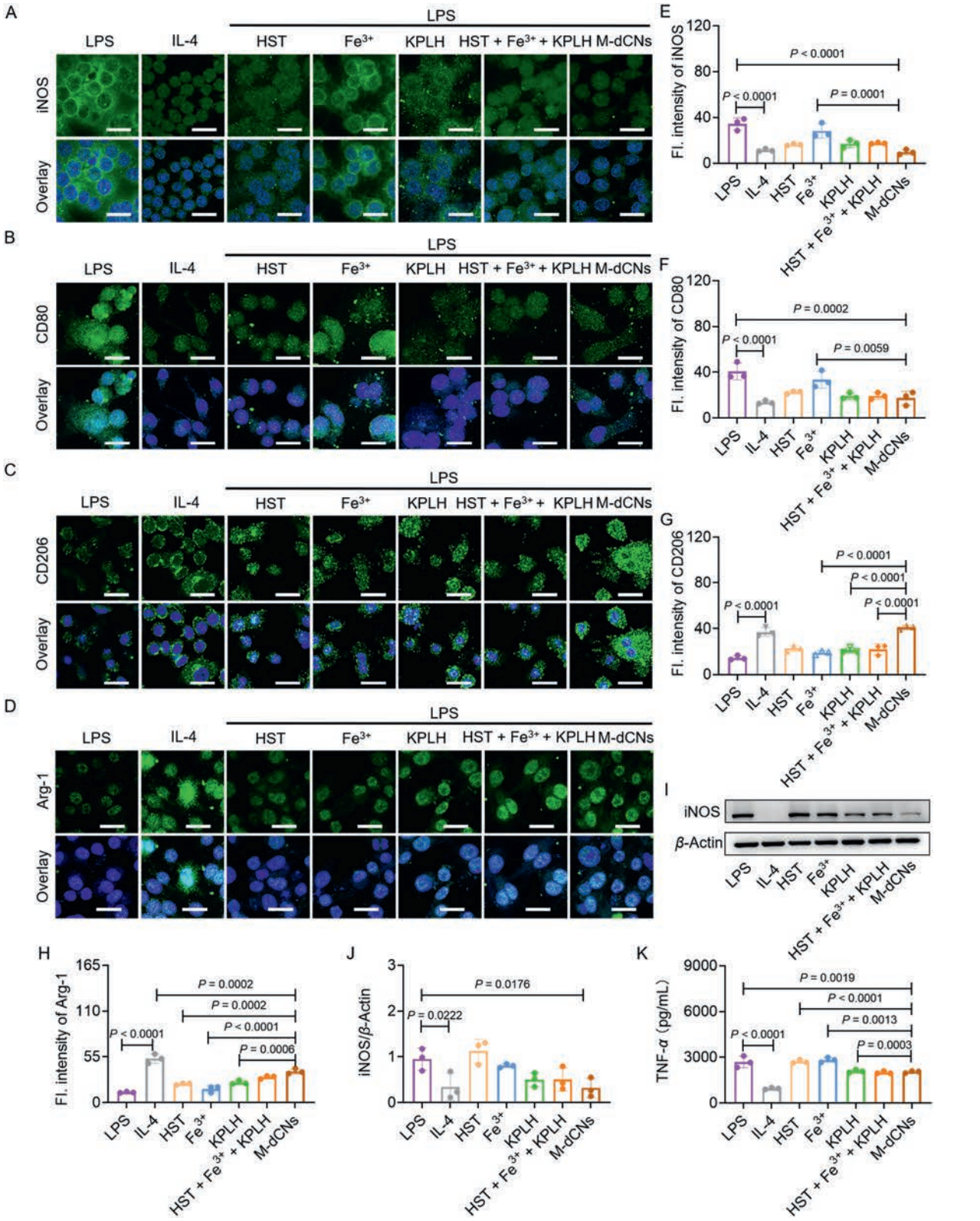

Figure 3 Representative immunofluorescence staining images of (A) iNOS, (B) CD80, (C) CD206 and (D) Arg1 in LPS-pretreated Kupffer cells after treatment with HST, Fe^{3+}, KPLH, HST + Fe^{3+} + KPLH or M-dCNs. Scale bar = 20 μm. Corresponding quantitative immunofluorescence analysis of (E) iNOS, (F) CD80, (G) CD206 and (H) Arg1 in Kupffer cells after those treatments. (I) Western blot analysis and (J) corresponding quantitative analysis of iNOS on Kupffer cells after those treatments. (K) Detection of TNF-α after LPS-pretreated Kupffer cells treatment with HST, Fe^{3+}, KPLH, HST + Fe^{3+} + KPLH or M-dCNs ($n = 3$). Data are presented as mean ± SD. *P* values were tested *via* a one-way ANOVA analysis.

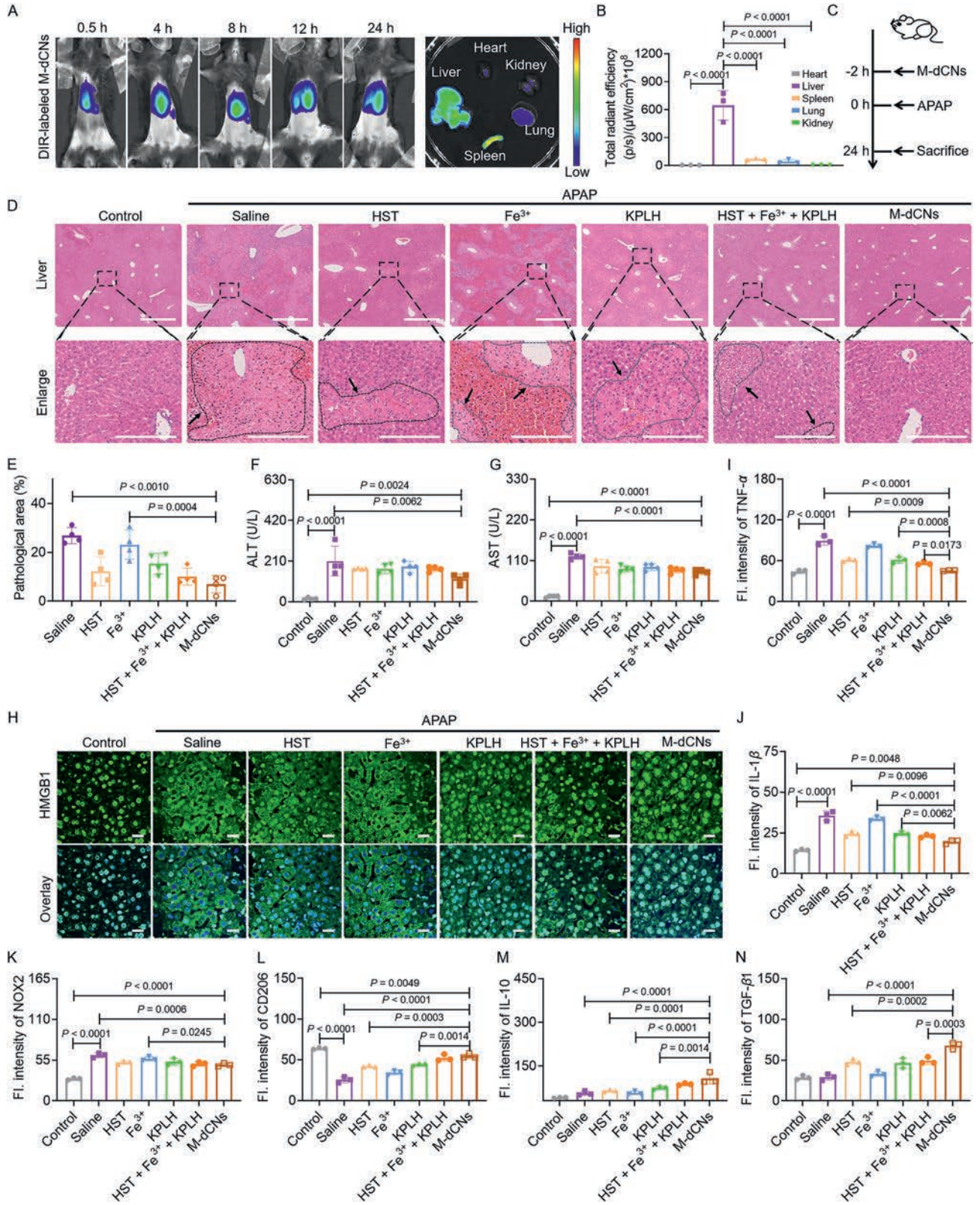

Figure 4 Biodistribution and the hepatoprotective effect of M-dCNs against early DILI *in vivo*. (A) Fluorescence images of DILI mice after intravenous injection with DiR-labeled M-dCNs for 0.5, 4, 8, 12, and 24 h as well as the *ex vivo* tissue images of mice after 24 h postinjection. (B) Corresponding quantitative analysis of DiR in various tissues ($n = 3$). (C) Experimental scheme of M-dCNs and APAP treating strategy in mice. (D) Representative H&E staining of liver sections from early DILI mice treated with saline, HST, Fe^{3+}, KPLH, HST + Fe^{3+} + KPLH or M-dCNs. Scale bar = 200 μm. (E) Quantification of necrotic areas by Image J software. (F) Serum ALT and (G) AST levels at 24 h after APAP intoxication indicated the hepatoprotective effect of different treatments on DILI ($n = 4$). (H) Representative HMGB1 (green) staining of liver sections. Scale

rapid compared to that at ambient temperature (25 °C). The cumulative release of HST reached 98.5 ± 2.5% within 2 h, while that of KPLH reached 86.6 ± 2.2%. This enhancement could be attributed to the increased thermal kinetic energy of both drug and water molecules, which intensified molecular motion and significantly accelerated the diffusion rate[52−54]. Furthermore, antioxidant activity assays demonstrated that M-dCNs showed 2.49-fold and 3.25-fold enhancements in •DPPH and hydroxyl radical (•OH) scavenging capacities, respectively, compared to free HST, confirming their robust nanozymatic ROS-scavenging performance (Fig. 1H and I). Based on these findings, we further evaluated the enzyme-like activities of M-dCNs. As shown in Supporting Information Fig. S7A−S7D, superoxide anions generated by the xanthine/xanthine oxidase system were effectively suppressed by M-dCNs, indicating SOD-mimetic activity that catalyzed the dismutation of $O_2^{\bullet-}$ into H_2O_2 and O_2. The SOD enzyme activity of M-dCNs was quantified as 37.35 U/mg. Using a catalase assay kit, we also examined the CAT-like activity of M-dCNs. Results showed that M-dCNs catalyzed the decomposition of H_2O_2, confirming a catalase-mimicking behavior analogous to that of natural catalase, with a determined CAT enzyme activity of 122.68 U/mg (Fig. S7E). From the Lineweaver-Burk double-reciprocal plot, the Michaelis constant (K_m) and maximum reaction rate (V_{max}) for the CAT-like activity were calculated as 38.61 mmol/L and 0.00568 mmol/(L·min), respectively. These kinetic parameters aligned with those reported for other iron-based nanozymes (Fig. S7F)[55]. Together, these results indicated that the dual SOD/CAT-like activities of M-dCNs possessed significant potential for application in the treatment of acute liver injury. Overall, these results validated the successful fabrication of stable, structurally uniform M-dCNs with unique antioxidant properties. Considering particle size distribution and colloidal stability, the formulation with a mass ratio of 3:2:2 for HST:Fe^{3+}:KPLH was selected for subsequent investigations.

3.2. Cellular uptake behavior and ROS scavenging ability of M-dCNs

To evaluate the intracellular drug delivery ability of M-dCNs in different liver cell types, AML12 (hepatocytes) and Kupffer cells were co-incubated with M-dCNs, respectively. Time-dependent uptake was observed in both cell types, with the fluorescence intensities at 8 h exceeding those at 2 h by 2.73-fold in AML12 cells and 1.22-fold in Kupffer cells (Fig. 2A and B, Supporting Information Fig. S8A and S8B). Furthermore, flow cytometry corroborated these findings, showing a progressive intracellular accumulation of M-dCNs (Fig. 2C and D, Fig. S8C and S8D). Moreover, MTT assays confirmed the negligible cytotoxicity of M-dCNs toward both cell lines at the tested doses after 24 h exposure (Fig. 2E and F). On this basis, DCFH-DA fluorescence assays revealed that M-dCNs effectively reduced APAP-induced ROS production by 85.36% in AML12 cells and 84.02% in Kupffer cells compared to the APAP-only groups (Fig. 2G−J). As a first-line clinical medication for liver injury, NAC served as a positive control to evaluate the concentration-dependent effect of M-dCNs on ROS clearance. As shown in Supporting Information Fig. S9A and S9B, following APAP pretreatment in hepatocytes, both NAC (100 μmol/L) and M-dCNs at three tested concentrations effectively downregulated DCF fluorescence expression, with M-dCNs demonstrating a concentration-dependent enhancement in ROS scavenging efficiency. A same trend was also confirmed in Kupffer cells (Fig. S9C and S9D). Additionally, Annexin V/PI staining demonstrated that M-dCNs significantly attenuated APAP-triggered apoptosis in AML12 cells, rising the cell viability rate from 33.59% to 61.93% (Fig. 2K and L). Consistent conclusions were obtained from MTT results processed using the same experimental procedure (Supporting Information Fig. S10). In summary, M-dCNs displayed efficient uptake by both hepatocytes and Kupffer cells and exhibited nanozyme-like catalytic activity capable of robust ROS elimination, ultimately mitigating hepatocyte damage.

3.3. Anti-inflammatory mechanism of M-dCNs

In the context of liver injury, the modulation of inflammation plays a pivotal role in determining therapeutic outcomes. Specifically, hepatic macrophages (Kupffer cells), particularly those polarized toward a pro-inflammatory (M1) phenotype, have been shown to exacerbate the early-phase inflammatory cascades. Consequently, reprogramming these M1 macrophages into an anti-inflammatory (M2) phenotype has emerged as a critical strategy for mitigating liver injury. To evaluate the potential of M-dCNs in driving Kupffer cells polarization from the M1 to M2 phenotype, immunofluorescence staining was performed to assess the expression of M1 key markers iNOS, CD80, and M2 key markers CD206, Arg1 in LPS-stimulated Kupffer cells. CLSM revealed intense green fluorescence corresponding to M1 markers in the LPS-treated cells, indicating a clear pro-inflammatory response (Fig. 3A and B). Conversely, IL-4 stimulation induced robust expression of CD206 and Arg1, further confirming the shift to the M2 phenotype (Fig. 3C and D). Notably, in LPS-induced Kupffer cells, the expression of iNOS and CD80 in HST, Fe^{3+}, KPLH, HST + Fe^{3+} + KPLH, and M-dCNs groups were 1.43, 2.48, 1.5, 1.54, 0.86 times higher and 1.6, 2.4, 1.4, 1.4, 1.3 times higher, respectively, compared to the IL-4 group (Fig. 3E and F). Strikingly, M-dCNs treatment led to a significant upregulation of CD206 (2.8-fold vs. LPS) and Arg1 (3.0-fold *vs*. LPS), strongly indicating M2 polarization (Fig. 3G and H). Concentration-dependent polarization effects were consistently observed with M-dCNs (Supporting Information Fig. S11A−S11D). Western blot further corroborated these findings, showing a remarkable 3-fold reduction in iNOS expression in M-dCNs-treated cells compared to the LPS controls (Fig. 3I and J). Additionally, M-dCNs treatment suppressed LPS-induced TNF-α secretion by 1.3-fold, further reinforcing their anti-inflammatory effects (Fig. 3K). The target of KPLH was validated, and downregulation of PDK expression was observed in all groups containing KPLH (Fig. S11E). Collectively, these data validated the potent anti-inflammatory properties of M-dCNs, which exerted their effects through the reprogramming of macrophage phenotypes and regulation of pro-inflammatory cytokines. These results supported the therapeutic potential of M-dCNs in APAP-induced liver injury by modulating hepatic inflammation.

bar = 20 μm. Corresponding quantitative analysis of (I) TNF-α, (J) IL-1β, (K) NOX2, (L) CD206, (M) IL-10 and (N) TGF-β1 after early DILI mice treatment with saline, HST, Fe^{3+}, KPLH, HST + Fe^{3+} + KPLH or M-dCNs by CLSM (n = 3). Data are presented as mean ± SD. P values were tested *via* a one-way ANOVA analysis.

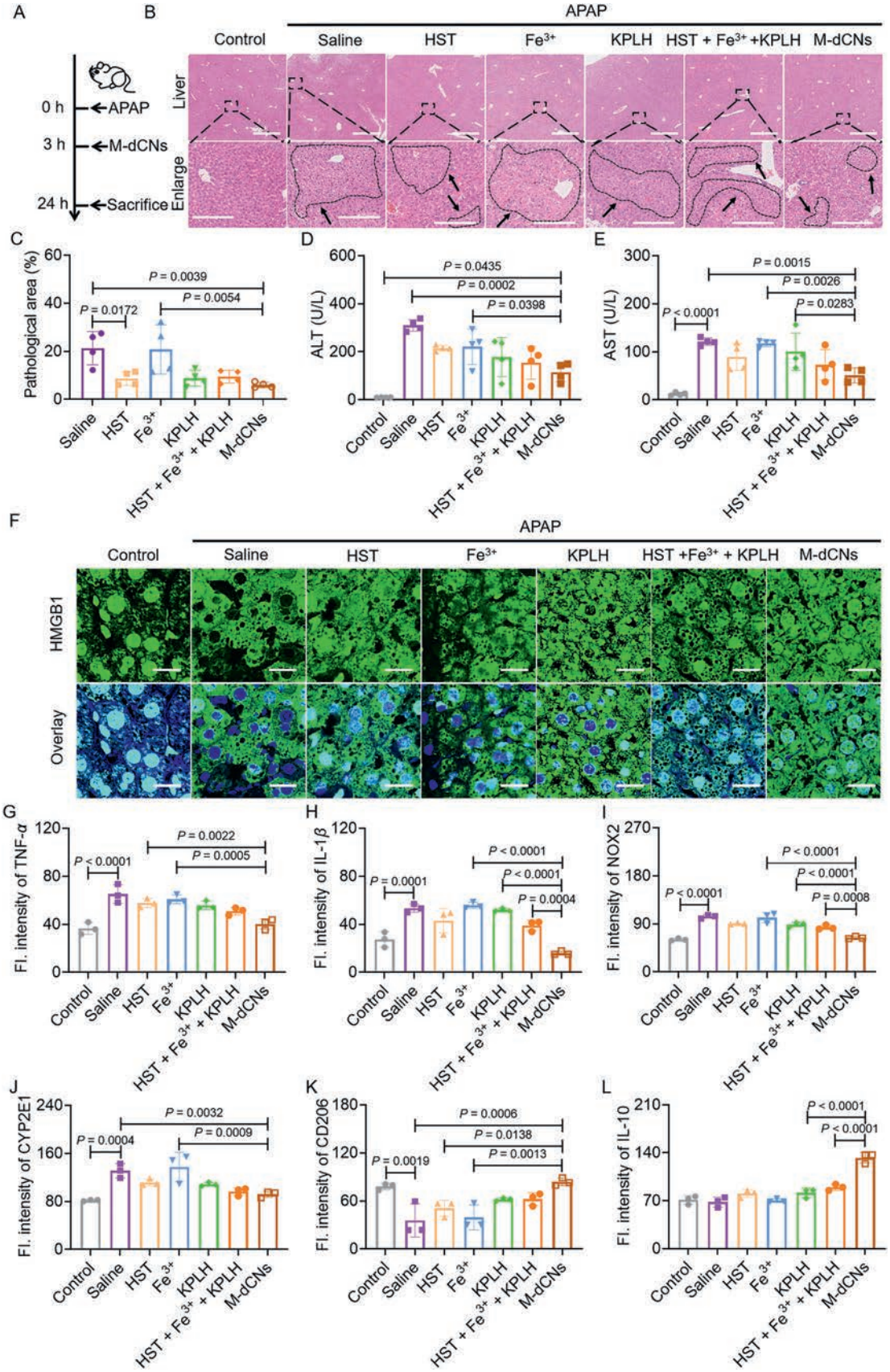

Figure 5 Therapeutic effect of M-dCNs in treating APAP-induced DILI at the advanced stages. (A) Experimental scheme of APAP and M-dCNs treating strategy in mice. (B) Representative H&E staining of liver sections from late DILI mice after treated with saline, HST, Fe^{3+},

3.4. Biodistribution and hepatoprotective potential of M-dCNs

The macrophage-polarizing and anti-inflammatory properties of M-dCNs motivated further investigation into their hepatoprotective potential *in vivo*. Prior to assessing therapeutic efficacy, the biodistribution of M-dCNs was examined. As shown in Fig. 4A and B, real-time fluorescence imaging revealed a pronounced liver-targeting capability, with hepatic fluorescence intensity exceeding that of the heart, spleen, lungs, and kidneys by 138.42-, 9.43-, 15.05-, and 60.33-fold, respectively. This remarkable hepatic accumulation was likely attributable to nonspecific nanoparticle uptake by Kupffer cells. Co-localization studies using CD11b (a Kupffer cell marker) and transferrin (an AML12 hepatocyte marker) confirmed the intracellular uptake of DiR-labeled M-dCNs by both cell types (Supporting Information Fig. S12). These findings underscored the passive liver-targeting capability of M-dCNs and their efficient accumulation in both hepatocytes and liver-resident macrophages *in vivo*, thereby indicating strong therapeutic potential for the alleviation of DILI.

To further explore the hepatoprotective potential of M-dCNs, the mice were treated with M-dCNs by intravenous injection 2 h before the APAP administration and the injury severity of liver was evaluated at 24 h after the APAP intoxication (Fig. 4C). As shown in Fig. 4D and E, histopathological analysis *via* H&E staining revealed severe liver damage in APAP-treated mice, with a necrotic area of 26.85%. Additionally, pre-administered mice showed varying degrees of relief in liver injury. Specifically, the damage area decreased by 12.19%, 23.11%, 15.36%, and 10.04% after treatment with HST, Fe^{3+}, KPLH, and HST + Fe^{3+} + KPLH. However, this damage was significantly attenuated to 6.99% in the M-dCNs pre-treatment group. These histological improvements were corroborated by serum biomarker analysis, where M-dCNs treatment led to reductions of 43.74% and 34.78% in ALT and AST levels, respectively, compared to the APAP-only group (Fig. 4F and G). At the mechanistic level, immunofluorescence staining revealed nuclear retention of HMGB1 (a marker of cellular integrity) in the livers of M-dCNs-treated mice, in contrast to the cytoplasmic translocation of HMGB1 observed in APAP-damaged tissues (Fig. 4H). Furthermore, while the liver of APAP-treated mice exhibited significant granular degeneration, the livers from the M-dCNs-treated group displayed histopathological features more akin to normal liver tissue (Supporting Information Fig. S13). These findings confirmed the ability of M-dCNs to effectively mitigate DILI in a prophylactic manner.

As we know, macrophages play a pivotal role in regulating the inflammatory response[56]. Among which, M1 macrophages are known to secrete pro-inflammatory cytokines such as TNF-α and IL-1β, whereas M2 macrophages produce anti-inflammatory cytokines, including CD206, IL-10, and TGF-β1[57]. Additionally, NOX2 contributes to hepatic dysfunction by inducing oxidative stress and promoting ROS production[58]. To further evaluate the role of M-dCNs in modulating the inflammatory response in DILI, the levels of pro-inflammatory cytokines (TNF-α, IL-1β, NOX2) and anti-inflammatory markers (CD206, IL-10, TGF-β1) were analyzed through immunofluorescence staining (Supporting Information Fig. S14). As shown in Fig. 4I−K, M-dCNs treatment significantly reduced the levels of pro-inflammatory mediators TNF-α, IL-1β, and NOX2 by 49.12%, 44.90%, and 21.14%, respectively, compared to the APAP-only group. In contrast, anti-inflammatory cytokines such as CD206, IL-10, and TGF-β1 were upregulated by 1.91- to 2.34-fold in the M-dCNs-treated group (Fig. 4L−N). Collectively, these findings verified that M-dCNs exerted hepatoprotective effects against DILI by attenuating oxidative stress, promoting macrophage polarization, and suppressing the production of inflammatory cytokines.

3.5. Therapeutic potential of M-dCNs in advanced acetaminophen (APAP) induced liver injury

In clinical practice, DILI commonly arises from unintentional APAP overdose, often exacerbated by delayed diagnosis and treatment[59]. Such scenarios frequently progress beyond the window of effective early intervention, underscoring the urgent need for therapeutics capable of mitigating advanced-stage liver injury. Building on the prophylactic efficacy of M-dCNs demonstrated in early APAP induced liver injury models, we next explored their therapeutic potential in more advanced stages of liver injury. As shown in Fig. 5A, the mice were treated with M-dCNs at 3 h after APAP intoxication, and we observed marginal therapeutic benefits conferred by M-dCNs at 24 h after the APAP intoxication. Histopathological evaluation *via* H&E staining revealed extensive hepatocellular necrosis and architectural disruption in livers from APAP-treated mice. Remarkably, these pathological hallmarks were markedly attenuated following M-dCNs administration, as evidenced by substantial restoration of tissue morphology (Fig. 5B). Quantitatively, the necrotic area was reduced by 72.06% in M-dCNs-treated mice compared to APAP-only controls (Fig. 5C). Biochemical analyses further reinforced the histological findings, with serum levels of ALT and AST (key indicators of liver injury) reduced by 63.05% and 58.05%, respectively, in the M-dCNs-treated group (Fig. 5D and E). These results indicated that M-dCNs possessed therapeutic potential for alleviating advanced-stage liver injury.

To investigate the underlying mechanisms, we also employed CLSM imaging to assess the intracellular localization of HMGB1. In APAP-damaged livers, significant HMGB1 cytoplasmic translocation was observed, indicating loss of nuclear integrity and extensive hepatocyte damage. Conversely, M-dCNs treatment preserved nuclear HMGB1 localization, thereby confirming their cytoprotective effects at the molecular level (Fig. 5F). Given the central role of inflammation in the progression of late-stage DILI, we further examined the immunomodulatory capability of M-dCNs. APAP metabolism, primarily mediated by cytochrome P450 enzyme CYP2E1, is known to generate reactive metabolites that initiate oxidative stress and inflammatory signaling cascades[60]. Therefore, we analyzed both macrophage polarization markers (iNOS for M1 and CD206 for M2 phenotypes) and a

KPLH, HST + Fe^{3+} + KPLH or M-dCNs. Scale bar = 200 μm. (C) Quantification of necrotic areas by Image J software. (D) Serum ALT and (E) AST levels at 24 h after APAP intoxication indicated the hepatoprotective effect of different treatments on DILI at the advanced stages (n = 4). (F) Representative HMGB1 (green) staining of liver sections. Scale bar = 20 μm. Corresponding quantitative analysis of (G) TNF-α, (H) IL-1β, (I) NOX2, (J) CYP2E1, (K) CD206, and (L) IL-10 after late DILI mice treatment with saline, HST, Fe^{3+}, KPLH, HST + Fe^{3+} + KPLH or M-dCNs by CLSM (n = 3). Data are presented as mean ± SD. P values were tested *via* a one-way ANOVA analysis.

panel of inflammatory mediators, including TNF-α, IL-1β, NOX2, CYP2E1, and the anti-inflammatory cytokine IL-10 (Supporting Information Fig. S15A). Immunofluorescence staining revealed that M-dCNs treatment normalized iNOS expression, showing a 1.69-fold reduction compared to APAP controls, indicative of suppressed pro-inflammatory M1 macrophage activation (Fig. S15B). In parallel, levels of TNF-α, IL-1β, NOX2, and CYP2E1 were significantly downregulated by 38.30%, 70.11%, 38.36%, and 29.87%, respectively, reflecting the broad anti-inflammatory and antioxidative capacity of M-dCNs (Fig. 5G−J). Importantly, the M2 macrophage marker CD206, which was diminished by 54.39% in APAP-treated livers, was fully restored to baseline levels following M-dCNs intervention (Fig. 5K). Concurrently, the anti-inflammatory cytokine IL-10 increased by 1.95-fold, further confirming a shift toward a reparative immune microenvironment (Fig. 5L). Consistent with observations in early-stage models, livers from APAP-treated mice displayed pronounced granular degeneration-an indicator of widespread cellular injury-whereas those treated with M-dCNs exhibited histological features more closely resembling healthy tissue (Supporting Information Fig. S16). Additionally, the therapeutic efficacy of NAC as a positive control was evaluated alongside the concentration-dependent effects of M-dCNs. Both NAC and varying concentrations of M-dCNs effectively reduced AST and ALT levels (Supporting Information Fig. S17A and S17B). The therapeutic effect of NAC at 300 mg/kg was comparable to that of low-dose M-dCNs (11.67 mg/kg), whereas high-dose M-dCNs (20 mg/kg) demonstrated the most pronounced protective effect against liver injury, showing a statistically significant advantage over NAC. Consistent conclusions were also obtained from the statistical analysis of pathological areas (Fig. S17C and S17D). These comprehensive findings demonstrated the potent therapeutic efficacy of M-dCNs in mitigating advanced DILI, achieved through dual mechanisms of oxidative stress suppression and immunological reprogramming toward a tissue-restorative phenotype.

3.6. Biosafety assessment of M-dCNs

To assess the translational potential of M-dCNs, their biosafety profile was systematically evaluated through histological examination and serum biochemical analysis in DILI mice administered with free HST, Fe^{3+}, KPLH, HST + Fe^{3+} + KPLH, or M-dCNs in 24 h. H&E staining of major organs, including the heart, liver, spleen, lungs, and kidneys, verified no discernible histopathological alterations or signs of off-target toxicity in any treatment group (Supporting Information Fig. S18A). In parallel, serum levels of hepatic and renal function markers (ALT, AST, UREA, and UA) remained within normal physiological ranges (Fig. S18B−S18E). Even at the highest concentration (20 mg/kg), no significant damage to major organs was observed in mice treated with M-dCNs over 7 and 14 days (Fig. S18F). Furthermore, all blood biochemical indicators, including AST, ALT, CRE, and bilirubin, maintained within normal ranges (Fig. S18G−S18J). Finally, the pharmacokinetic profile of DiR-labeled M-dCNs was investigated. As shown in Supporting Information Fig. S19A and S19B and Table S6, compared with free DiR, DiR-labeled M-dCNs exhibited a larger area under the concentration-time curve (AUC) and a longer half-life ($t_{1/2}$), although both were completely metabolized within 24 h, collectively demonstrating the excellent systemic biocompatibility and favorable safety profile of M-dCNs.

4. Conclusions

In summary, a metal−drug coordinated nanozyme (M-dCNs) was developed for the effective mitigation of DILI. The coordination among ferric ions, HST, and KPLH enabled the formation of M-dCNs with uniform particle size distribution and enhanced structural stability. Notably, M-dCNs demonstrated intrinsic antioxidant enzyme-mimetic activity, allowing efficient scavenging of intracellular ROS within hepatocytes, thereby alleviating oxidative damage associated with DILI. In parallel, M-dCNs reprogrammed hepatic macrophages toward an anti-inflammatory phenotype, significantly suppressing the secretion of pro-inflammatory cytokines and downstream inflammatory responses. By leveraging both antioxidant and immunomodulatory mechanisms, M-dCNs exhibited potent hepatoprotective efficacy, facilitating the repair of necrotic hepatic lesions and mitigating oxidative stress and immune cell infiltration. Overall, this work highlighted a metal−drug coordinated nanozyme platform as a promising and synergistic approach for the treatment of DILI through the dual regulation of redox balance and inflammatory microenvironment remodeling.

Acknowledgments

This work was financially supported by the National Natural Science Foundation of China (32371394 and 82574881), the National Key R&D Program of China (2021YFD1800600), the Guangdong Basic and Applied Basic Research Foundation (2023A1515140078, 2023B1515120079, and 2024A1515030229), the Guangdong Special Support Program (No. 0720240250), and the Scientific and Technological Project of Guangzhou in 2024 (No. 2024B03J0037).

Author contributions

Xiayun Chen and Shiying Li designed the research. Xiayun Chen, Ziqi Liang, Lichong Lu, and Zhouchuan Shao carried out the experiments. Xiayun Chen performed data analysis and wrote the manuscript. Wenhui Tang, Yiqi Liu, Jianqiao Li, and Enping Lai participated part of the experiments. Shiying Li, Minyan Wei, Guodong Zheng, and Baizhong Chen provided quality control and revised the manuscript. All of the authors have read and approved the final manuscript.

Conflicts of interest

The authors declare no conflicts of interest.

Appendix A. Supporting information

Supporting information to this article can be found online at https://doi.org/10.1016/j.apsb.2026.05.006.

References

1. Stravitz RT, Lee WM. Acute liver failure. *Lancet* 2019;**394**:869−81.
2. Liu HY, Yin G, Kohlhepp MS, Schumacher F, Hundertmark J, Hassan MIA, et al. Dissecting acute drug-induced hepatotoxicity and therapeutic responses of steatotic liver disease using primary mouse liver and blood cells in a liver-on-a-chip model. *Adv Sci* 2024;**11**: e2403516.

3. Yan MZ, Huo YZ, Yin ST, Hu HB. Mechanisms of acetaminophen-induced liver injury and its implications for therapeutic interventions. *Redox Biol* 2018;**17**:274−83.
4. Segovia-Zafra A, Di Zeo-Sánchez DE, López-Gómez C, Pérez-Valdés Z, García-Fuentes E, Andrade RJ, et al. Preclinical models of idiosyncratic drug-induced liver injury (iDILI): moving towards prediction. *Acta Pharm Sin B* 2021;**11**:3685−726.
5. Chao XJ, Niu MW, Wang SG, Ma XW, Yang X, Sun H, et al. High-throughput screening of novel TFEB agonists in protecting against acetaminophen-induced liver injury in mice. *Acta Pharm Sin B* 2024;**14**:190−206.
6. Du K, Ramachandran A, Jaeschke H. Oxidative stress during acetaminophen hepatotoxicity: sources, pathophysiological role and therapeutic potential. *Redox Biol* 2016;**10**:148−56.
7. Andrade RJ, Chalasani N, Björnsson ES, Suzuki A, Kullak-Ublick GA, Watkins PB, et al. Drug-induced liver injury. *Nat Rev Dis Primers* 2019;**5**:58.
8. Jaeschke H, Adelusi OB, Akakpo JY, Nguyen NT, Sanchez-Guerrero G, Umbaugh DS, et al. Recommendations for the use of the acetaminophen hepatotoxicity model for mechanistic studies and how to avoid common pitfalls. *Acta Pharm Sin B* 2021;**11**:3740−55.
9. Krenkel O, Tacke F. Liver macrophages in tissue homeostasis and disease. *Nat Rev Immunol* 2017;**17**:306−21.
10. Wang Q, Jiang QK, Li D, Yang ZM, Gao L, Liu F, et al. Elaborately engineering of lipid nanoparticle for targeting delivery of siRNA and suppressing acute liver injury. *Chin Chem Lett* 2024;**35**:108683.
11. Li FY, Qiu YP, Xia F, Sun H, Liao HW, Xie A, et al. Dual detoxification and inflammatory regulation by ceria nanozymes for drug-induced liver injury therapy. *Nano Today* 2020;**35**:100925.
12. Guan F, Wang RX, Yi ZJ, Luo P, Liu WY, Xie Y, et al. Tissue macrophages: origin, heterogeneity, biological functions, diseases and therapeutic targets. *Signal Transduct Targeted Ther* 2025;**10**:93.
13. Han ZH, Gao X, Wang YJ, Cheng SN, Zhong XY, Xu Y, et al. Ultrasmall iron-quercetin metal natural product nanocomplex with antioxidant and macrophage regulation in rheumatoid arthritis. *Acta Pharm Sin B* 2023;**13**:1726−39.
14. Shan J, Jin X, Zhang C, Huang MC, Xing JH, Li QR, et al. Metal natural product complex Ru-procyanidins with quadruple enzymatic activity combat infections from drug-resistant bacteria. *Acta Pharm Sin B* 2024;**14**:2298−316.
15. Hua P, Liang RF, Tu YB, Yin YY, Law MK, Chen MW. Reactive oxygen species and nitric oxide scavenging nanoparticles alleviating rheumatoid arthritis through adjusting the seeds and growing soils. *Acta Pharm Sin B* 2023;**13**:5016−29.
16. Geervliet E, Arora S, Donohue D, Pinheiro de Albuquerque CA, Terstappen LW, Schasfoort R, et al. Design, molecular characterization and therapeutic investigation of a novel CCR8 peptide antagonist that attenuates acute liver injury by inhibiting infiltration and activation of macrophages. *Acta Pharm Sin B* 2025;**15**:2114−33.
17. Fan XQ, Mai CT, Zuo L, Huang JM, Xie C, Jiang ZB, et al. Herbal formula Ba Wei Bai Du San alleviates polymicrobial sepsis-induced liver injury *via* increasing the gut microbiota *Lactobacillus johnsonii* and regulating macrophage anti-inflammatory activity in mice. *Acta Pharm Sin B* 2023;**13**:1164−79.
18. Hu Q, Lyon CJ, Fletcher JK, Tang WF, Wan MH, Hu TY. Extracellular vesicle activities regulating macrophage- and tissue-mediated injury and repair responses. *Acta Pharm Sin B* 2021;**11**:1493−512.
19. Wang Q, Wan B, Feng Y, Yang ZM, Li D, Liu F. Self-degradable "gemini-like" ionizable lipid-mediated delivery of siRNA for subcellular-specific gene therapy of hepatic diseases. *Acta Pharm Sin B* 2025;**15**:2867−83.
20. Pawlak M, Lefebvre P, Staels B. Molecular mechanism of PPARα action and its impact on lipid metabolism, inflammation and fibrosis in non-alcoholic fatty liver disease. *J Hepatol* 2015;**62**:720−33.
21. Aoyama T, Inokuchi S, Brenner DA, Seki E. CX3CL1−CX3CR1 interaction prevents carbon tetrachloride-induced liver inflammation and fibrosis in mice. *Hepatology* 2010;**52**:1390−400.
22. Addolorato G, Mirijello A, Barrio P, Gual A. Treatment of alcohol use disorders in patients with alcoholic liver disease. *J Hepatol* 2016;**65**:618−30.
23. Song L, Cao LJ, Liu R, Ma H, Li YN, Shang QW, et al. The critical role of T cells in glucocorticoid-induced osteoporosis. *Cell Death Dis* 2020;**12**:45.
24. Foretz M, Guigas B, Viollet B. Metformin: update on mechanisms of action and repurposing potential. *Nat Rev Endocrinol* 2023;**19**:460−76.
25. Palmieri EM, Gonzalez-Cotto M, Baseler WA, Davies LC, Ghesquière B, Maio N, et al. Nitric oxide orchestrates metabolic rewiring in M1 macrophages by targeting aconitase 2 and pyruvate dehydrogenase. *Nat Commun* 2020;**11**:698.
26. Sun K, Fan JY, Han JY. Ameliorating effects of traditional Chinese medicine preparation, Chinese materia medica and active compounds on ischemia/reperfusion-induced cerebral microcirculatory disturbances and neuron damage. *Acta Pharm Sin B* 2015;**5**:8−24.
27. Yin JQ, Ma LL, Wang HQ, Yan HY, Hu J, Jiang W, et al. Chinese herbal medicine compound Yi-Zhi-Hao Pellet inhibits replication of influenza virus infection through activation of heme oxygenase-1. *Acta Pharm Sin B* 2017;**7**:630−7.
28. Wang LQ, Yang R, Yuan BC, Liu Y, Liu CS. The antiviral and antimicrobial activities of licorice, a widely-used Chinese herb. *Acta Pharm Sin B* 2015;**5**:310−5.
29. Yin LZ, Jiang XW, Wang M, Yang YR, He ZG, Sun J, et al. Phytoconstituent-derived nano-medicines/vesicles providing a promising dawn for inflammatory bowel disease. *Chin Chem Lett* 2024;**36**:110224.
30. He J, Du JX, Wang M, Luo XD, Feng T. Irpexlactones A and B, a pair of ring-rearranged tremulane sesquiterpenoids from the basidiomycete *Irpex lacteus* and their anti-inflammatory activity. *Chin Chem Lett* 2024;**36**:110769.
31. Shao MY, Zhang XQ, Sun JM, Dong HY, Han X, Yang Q, et al. Saikosaponin b1 attenuates liver fibrosis by blocking STAT3/Gli1 interaction and inducing Gli1 degradation. *Explorations* 2025;**5**:70000.
32. Li ZY, Shen H, Cai WL, Xu QG, Xia W, Ning KK, et al. Colon-targeted pellets encapsulating patchouli oil cocrystal for inflammatory bowel disease treatment. *Chin Chem Lett* 2025:111292.
33. Zhang YY, Qiu L, Li HY, Cai WL, Liu EG, Zhang HT, et al. Biomimetically engineered plant-derived exosomes-like nanovesicles for rheumatoid arthritis therapy. *Chin Chem Lett* 2024;**36**:110658.
34. Zhen B, Suo XY, Dang J, Yue HL, Tao YD, Wang JJ, et al. Hyperterpenoids A and B: two pairs of unprecedented 6/6/4/6/6 polycyclic cyclobutane meroterpenoids with potent neuroprotective and anti-inflammatory activities from *Hypericum beanii*. *Chin Chem Lett* 2021;**32**:2338−41.
35. Polat FR, Karaboğa I. Immunohistochemical examination of anti-inflammatory and anti-apoptotic effects of hesperetin on trinitrobenzene sulfonic acid induced colitis in rats. *Biotech Histochem* 2019;**94**:151−8.
36. Muhammad T, Ikram M, Ullah R, Rehman SU, Kim MO. Hesperetin, a citrus flavonoid, attenuates LPS-induced neuroinflammation, apoptosis and memory impairments by modulating TLR4/NF-κB signaling. *Nutrients* 2019;**11**:648.
37. Miles EA, Calder PC. Effects of citrus fruit juices and their bioactive components on inflammation and immunity: a narrative review. *Front Immunol* 2021;**12**:712608.
38. Guo YX, Sun Q, Wu FG, Dai YL, Chen XY. Polyphenol-containing nanoparticles: synthesis, properties, and therapeutic delivery. *Adv Mater* 2021;**33**:e2007356.
39. Rodríguez-Arce E, Saldías M. Antioxidant properties of flavonoid metal complexes and their potential inclusion in the development of novel strategies for the treatment against neurodegenerative diseases. *Biomed Pharmacother* 2021;**143**:112236.
40. Gu JK, Zhang PY, Li HJ, Wang YS, Huang Y, Fan L, et al. Cerium-luteolin nanocomplexes in managing inflammation-related diseases by antioxidant and immunoregulation. *ACS Nano* 2024;**18**:6229−42.

41. Zhang QT, Li MF, Guo CY, Jia Z, Wan GC, Wang SF, et al. Fe_3O_4 nanoparticles loaded on lignin nanoparticles applied as a peroxidase mimic for the sensitively colorimetric detection of H_2O_2. *Nanomaterials* 2019;**9**:210.
42. Yu X, Wang YW, Zhang J, Liu J, Wang AZ, Ding LH. Recent development of copper-based nanozymes for biomedical applications. *Adv Healthcare Mater* 2024;**13**:e2302023.
43. Peng C, Pang RY, Li J, Wang EK. Current advances on the single-atom nanozyme and its bioapplications. *Adv Mater* 2024;**36**:e2211724.
44. Zou HY, Hong YZ, Xu BQ, Wang MT, Xie HY, Wang YJ, et al. Multifunctional cerium oxide nanozyme for synergistic dry eye disease therapy. *ACS Appl Mater Interfaces* 2024;**16**:34757−71.
45. Shen JC, Rees TW, Zhou ZG, Yang SP, Ji LN, Chao H. A mitochondria-targeting magnetothermogenic nanozyme for magnet-induced synergistic cancer therapy. *Biomaterials* 2020;**251**:120079.
46. Li YJ, Chai HN, Yuan ZS, Huang CN, Wang SS, Sun YJ, et al. Metal-organic framework-engineered enzyme/nanozyme composites: preparation, functionality, and sensing mechanisms. *Chem Eng J* 2024;**496**:153884.
47. Zheng RR, Zhao LP, Huang CY, Cheng H, Yang N, Chen ZX, et al. Paraptosis inducer to effectively trigger immunogenic cell death for metastatic tumor immunotherapy with IDO inhibition. *ACS Nano* 2023;**17**:9972−86.
48. Zheng RR, Zhao LP, Chen XY, Liu LS, Liu YB, Chen XT, et al. Metal-coordinated nanomedicine for combined tumor therapy by inducing paraptosis and apoptosis. *J Control Release* 2021;**336**:159−68.
49. Dai HL, Han T, Cui JT, Li X, Abbasi HN, Wang XG, et al. Stability, aggregation, and sedimentation behaviors of typical nano metal oxide particles in aqueous environment. *J Environ Manag* 2022;**316**:115217.
50. Liu JJ, Louie SM, Pham C, Dai C, Liang DL, Hu YD. Aggregation of ferrihydrite nanoparticles: effects of pH, electrolytes, and organics. *Environ Res* 2019;**172**:552−60.
51. Na K, Lee DH, Hwang DJ, Park HS, Lee KH, Bae YH. pH-sensitivity and pH-dependent structural change in polymeric nanoparticles of poly(vinyl sulfadimethoxine)−deoxycholic acid conjugate. *Eur Polym J* 2006;**42**:2581−8.
52. Chaban VV, Savchenko TI, Kovalenko SM, Prezhdo OV. Heat-driven release of a drug molecule from carbon nanotubes: a molecular dynamics study. *J Phys Chem B* 2010;**114**:13481−6.
53. Stergar J, Jirák Z, Veverka P, Kubíčková L, Vrba T, Kuličková J, et al. Mn-Zn ferrite nanoparticles coated with mesoporous silica as core material for heat-triggered release of therapeutic agents. *J Magn Magn Mater* 2019;**475**:429−35.
54. Tagami T, Ernsting MJ, Li SD. Efficient tumor regression by a single and low dose treatment with a novel and enhanced formulation of thermosensitive liposomal doxorubicin. *J Control Release* 2011;**152**:303−9.
55. Chen ZW, Yin JJ, Zhou YT, Zhang Y, Song LN, Song MJ, et al. Dual enzyme-like activities of iron oxide nanoparticles and their implication for diminishing cytotoxicity. *ACS Nano* 2012;**6**:4001−12.
56. Tu ZL, Chen M, Wang M, Shao ZX, Jiang XQ, Wang KY, et al. Engineering bioactive M2 macrophage-polarized anti-inflammatory, antioxidant, and antibacterial scaffolds for rapid angiogenesis and diabetic wound repair. *Adv Funct Mater* 2021;**31**:2100924.
57. Shiao SL, Kershaw KM, Limon JJ, You S, Yoon J, Ko EY, et al. Commensal bacteria and fungi differentially regulate tumor responses to radiation therapy. *Cancer Cell* 2021;**39**:1202−13.
58. Li HD, Chen X, Xu JJ, Zhu L, Li C, Sun XL, et al. GRP/GRPR enhances alcohol-associated liver injury through the IRF1-mediated caspase-1 inflammasome and NOX2-dependent ROS pathway. *Hepatology* 2024;**79**:392−408.
59. Larson AM, Polson J, Fontana RJ, Davern TJ, Lalani E, Hynan LS, et al. Acetaminophen-induced acute liver failure: results of a United States multicenter, prospective study. *Hepatology* 2005;**42**:1364−72.
60. Jaeschke H, McGill MR, Ramachandran A. Oxidant stress, mitochondria, and cell death mechanisms in drug-induced liver injury: lessons learned from acetaminophen hepatotoxicity. *Drug Metab Rev* 2012;**44**:88−106.